Supplementary Information

Controlling the ferroelectric and resistive switching properties of $BiFeO_3$ thin film prepared using sub – 5 nm dimension nanoparticles

Mandar M. Shirolkar[1,2,†], Jieni Li[1,3], Xiaolei Dong[1], Ming Li[1] and Haiqian Wang[1*]

[1]Hefei National Laboratory for Physical Sciences at the Microscale, University of Science and Technology of China, Hefei, Anhui 230026, People's Republic of China

[2]Department of Physics, Tamkang University, Tamsui, 251, Taiwan

[†] **mandar@ustc.edu.cn; mmshirolkar@gmail.com**

[3] Current Address: International Collaborative Laboratory of 2D Materials for Optoelectronics Science and Technology, College of Optoelectronic Engineering, Shenzhen University Shenzhen 518060, People's Republic of China

[*] Corresponding Author**: hqwang@ustc.edu.cn**

Thermogravimetric (TG) analysis of $BiFeO_3$ precursor

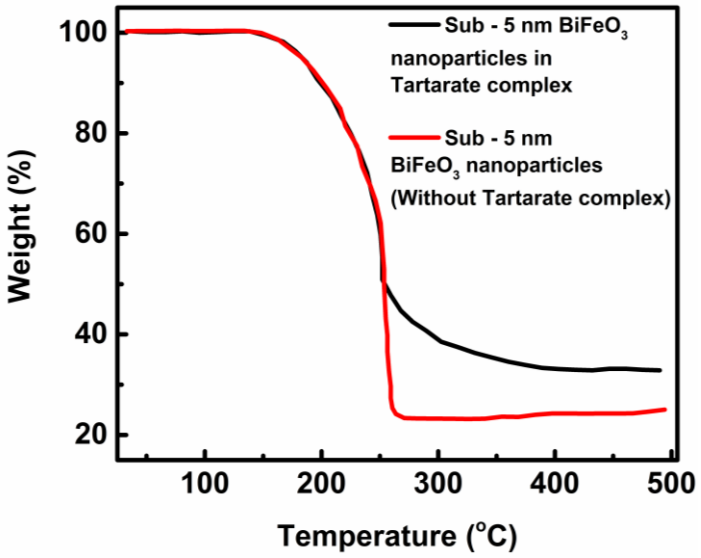

Figure S1 TG profiles of as prepared $BiFeO_3$ precursor at various preparation conditions.

Thermogravimetric analysis of the samples were obtained using NETZSCH Jupiter STA 449F3 instrument. The data was collected from 30°C to 500°C at a heating rate of 5°C/min under an artificial air atmosphere at pressure 60 sccm.

Small Angle X - ray scattering (SAXS) analysis

We performed SAXS experiment on the nanoparticles dispersion to access the effects of dispersion of $BiFeO_3$ sub – 5 nm NPs in water on the overall structure, over the whole length scale ranging from individual nanoparticle to the nanoclusters and nano – aggregate. SAXS measurement on sub – 5 nm $BiFeO_3$ nanoparticles (NPs) suspension in water was carried out on a laboratory SAXS instrument NanoStar, Bruker equipped with a microfocus Cu Kα X-ray source, collimating system with motorized scatterless slits (Xenocs, France), and HiStar 2D multiwire gas detector (Siemens/Bruker). SAXS pattern was collected with a beam size of 1 × 1 mm. The pattern was corrected for the detector's dark current and spatial distortion. Additionally, pattern was normalized using sample thickness, exposure time, sample transmission and the detector normalization coefficient and integrated using the Fit2D software.

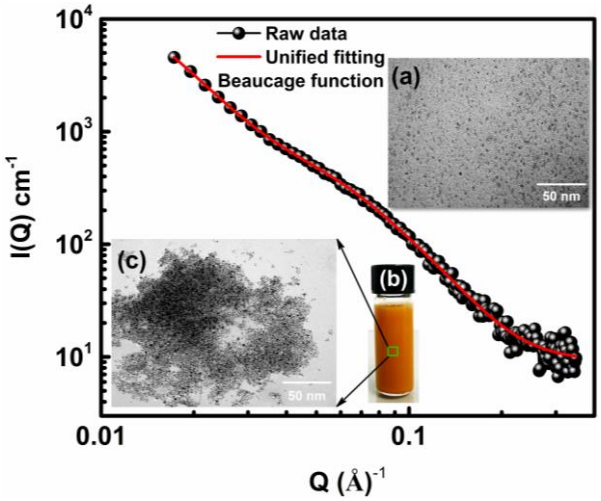

Figure S2 SAXS profile obtained on suspension of $BiFeO_3$ sub - 5 nm nanoparticles. The insets (a) TEM micrograph of as prepared tartarate free sub – 5 nm $BiFeO_3$ nanoparticles, (b) optical photograph of aqueous suspension of $BiFeO_3$ nanoparticles and (c) TEM micrograph of fractal like aggregates/clusters of $BiFeO_3$ suspended in water.

Figure S2 shows SAXS profile obtained on the $BiFeO_3$ nanoparticles suspension. The scattering profile fitted well with unified fitting approach described by Lee et al.,

suggesting that nanoparticles are aggregated and exhibit mass – fractal aggregation[1]. The mass - fractal aggregation has two structural levels, (i) the primary particles and (ii) the mass – fractal aggregates. Each structural level is described by the integrated approach with four universal parameters, $G, R_g, B,$ and $P,$ which can be calculated from limits of integral equations for the mass – fractals. The above parameters are defined as follows[1],

$$G_2 = N_{\mathrm{agg}} \Delta n_{\mathrm{e\,agg}}{}^2 = \left(N_{\mathrm{pp}}/z\right)\left(z\Delta n_{\mathrm{e\,pp}}\right)^2 = zN_{\mathrm{pp}}\left(\Delta n_{\mathrm{e\,pp}}\right)^2 = zG_1 \qquad (1)$$

where N_{agg} is the number of aggregates in the scattering volume, N_{pp} is the number of primary particles in the scattering volume, Δn_{epp} is a contrast factor for the primary particles and z is the degree of aggregation i.e. number of primary particles in an aggregate.

The radius of gyration R_g has two forms[1]:

(1) Primary particle radius of gyration (R_{g1}) is given by $R_{g1} = \left(3/5\right)^{1/2} R$, where R is radius of primary particle (considering single sub – 5 nm nearly spherical particle)

(2) Mass – fractal aggregate (R_{g2}), which is a function of mass – fractal dimension (d_f) and degree of aggregation z, express as

$$R_{g2} = \left\{b^2 z^{2/d_f} \Big/ \left[\left(1+2/d_f\right)\left(2+2/d_f\right)\right]\right\}^{1/2} \qquad (2)$$

where b is the primary particle size, b = 2R. B is prefactor specific to the type of power – law scattering, which has two forms B_1 and B_2 considering R_{g1} and R_{g2} respectively.

$$B_1 = N_{pp} 2\pi \left(\Delta n_{epp}^2 / V_{pp}^2\right) S_{pp} \qquad (3)$$

where n_{epp} is the number of electrons in a primary particle and V_{pp} is the volume of primary particle.

$$B_2 = \left(G d_f / R_{g2}^{d_f}\right)\Gamma\left(d_f/2\right) \qquad (4)$$

where Γ is the gamma function. The expression for B_2 is power – law prefactor for mass – fractal aggregates and define as $P = -d_f$

The above series of expressions are known as Beaucage function of second order. The scattering profile was fitted considering the above expressions, which yield the parameters R_{g1}, R_{g2}, df and z related to the $BiFeO_3$ nanoparticle suspension.

The obtained values are R_{g1} = 24.02 Å , R_{g2} = 501.03 Å , d_f = 1.83 and z = 23. Thus, analysis show that $BiFeO_3$ sub – 5 nm are aggregated to form a mass – fractal aggregate of an average size 100 nm from primary nanoparticles of an average dimension 3 nm.

X – ray photoelectron spectroscopy (XPS) studies

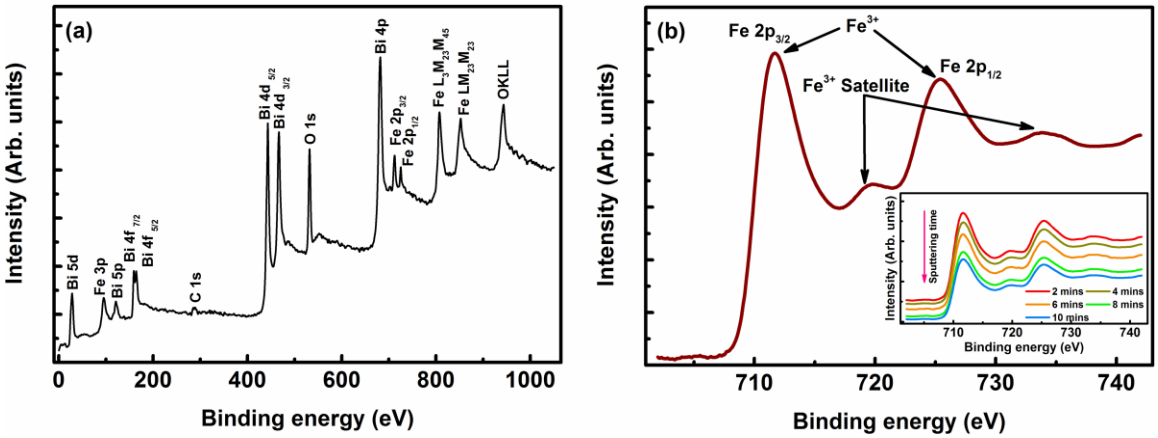

Figure S3 (a) XPS survey scan of all the $BiFeO_3$ sample indicating elements present in the sample and (b) The inset shows high resolution scan of Fe region.

XPS studies on the thin film sample was carried out using Thermo scientific ESCALAB 250 using Al Kα radiation source (1486.6 eV) and the base pressure of experimental chamber was ≈ 10^{-8} mbar during the experiments. The survey scan (Figure. S3(a)) shows the presence of Bi, Fe and O along with a small amount of C. The presence of carbon can be attributed to the sample preparation conditions, which was used for correcting the charging effect. Overall, the survey scan confirms the purity of BFO NPs. Figure S3(b) shows Fe 2p scan for $BiFeO_3$ thin film sample. It shows that the binding energies of spin – orbit doublets of Fe^{3+} at 711.3 eV ($2p_{3/2}$) and 723.8 eV ($2p_{1/2}$). The absence of peak corresponding to Fe^{2+} oxidation state of iron indicates the dominant role of Fe^{3+} ions for ferromagnetism in thin film[2]. We also performed depth profile analysis to evaluate the oxidation state of iron, which shows that with distance, Fe^{3+} oxidation state of iron in the thin film remains unaltered (see inset of Figure S3(b)).

Grazing incidence X – ray diffraction (GIXRD) analysis

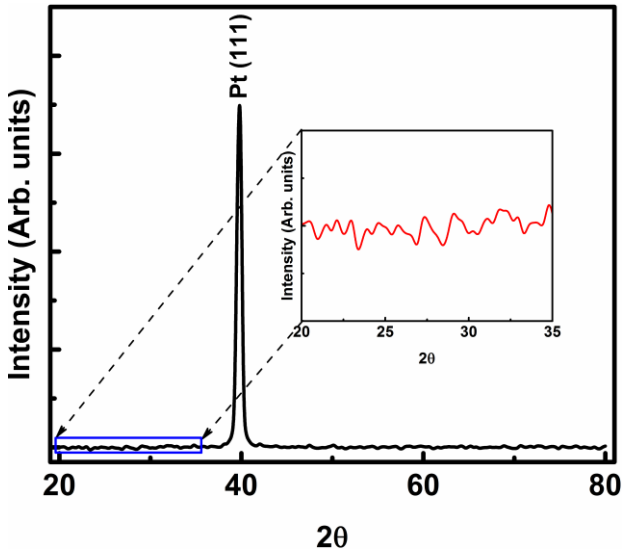

Figure S4 GIXRD pattern of as prepared BFO thin film on Pt/SiO_2 substrate. The inset shows magnified view of highlighted rectangle portion of XRD pattern, which shows that BFO thin film is X – ray amorphous in nature.

GIXRD patterns of the film was recorded using Panalytical X'Pert Pro (Cu-Kα ≈ 1.5406 Å, operated at 40 KV, current 40 mA and angle of incidence 0.5°. Data was collected in the range 2θ = 20° to 80° range with 0.02 step size and 10 s counting time.

Magneto – Raman spectroscopy

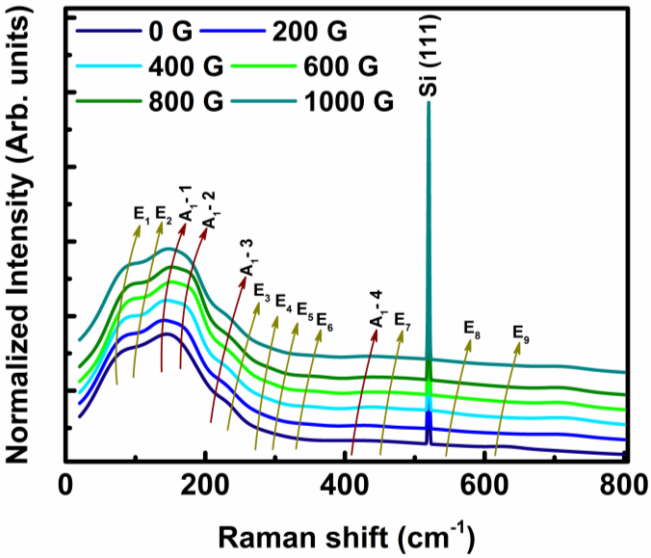

Figure S5 Magneto – Raman spectroscopy of BFO thin film on Si (111) substrates.

Table T1 Observed Raman modes for BFO thin films on Si(111) as a function of magnetic field. The reported Raman modes for BFO sub – 5 nm NPs are also shown for the reference.

Raman modes	Raman shift (cm^{-1})						
	$BiFeO_3$ NPs Sub – 5 nm^2	Magnetic Field (Gauss)					
		0	200	400	600	800	1000
A_1-1	138	140	145	148	152	155	159
A_1-2	172	173	174	176	178	180	182
A_1-3	221	222	222	223	223	223	222
A_1-4	428	428	429	429	428	429	429
E_1	62	69	72	76	80	83	86
E_2	100	102	105	108	110	113	115
E_3	262	262	265	265	265	265	265
E_4	291	291	291	292	292	292	292
E_5	339	340	340	341	340	341	341
E_6	361	362	362	361	362	362	362
E_7	473	475	475	475	475	475	475
E_8	522	523	523	523	523	523	523
E_9	621	623	623	623	623	623	623

Magnetic and magneto – capacitance or magneto – dielectric measurements

The magnetization measurements of the BFO NPs were carried out using a magnetic property measurement system (MPMS) from MPMS 3, Quantum Design Inc. San Diego, CA equipped with a 7 T superconducting magnet.

Magnetic field dependent dielectric measurements were performed using an Agilent 4284A LCR meter while the magnetic field was controlled by the above mentioned MPMS instrument.

Figure S6(a) shows room temperature magnetization measurements in the in – plane and out – of – plane modes. It can be seen that saturation magnetization in the in – plane configuration is 0.79 μ_B/Fe, while for out – of – plane configuration, it is 0.62 μ_B/Fe. The thin film shows coercivity 388 Oe and 213 Oe in the in – plane and out – of – plane configurations respectively, while exchange bias values were observed to be 51 Oe and 25 Oe in the in – plane and out – of – plane configurations respectively.

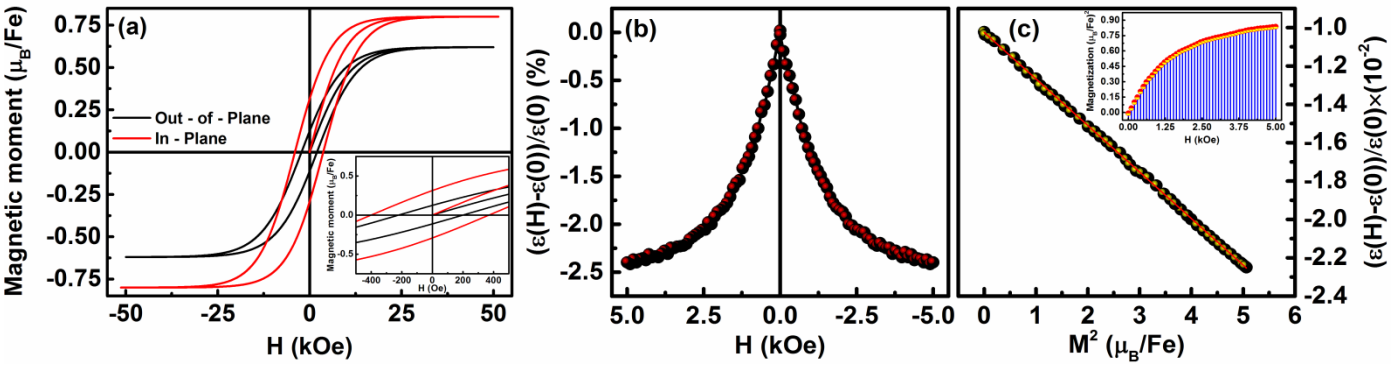

Figure S6 (a) Room temperature M – H measurement of the thin film in in – plane and out – of – plane configurations. The inset shows magnified part of central part of hysteresis loops representing coercivity and exchange bias, (b) magnetocapacitance effect of BFO thin film measured at 1 kHz frequency and (d) the variation of magnetocapacitance as a function M^2 for thin film. The inset shows variation of M^2 with an applied magnetic field.

The coupling between electric and magnetic polarizations has been investigated by room temperature magneto – capacitance (MC) or magneto – dielectric measurements.

Figure S6(b) shows change in the value of dielectric constant as a function of an applied magnetic field (H) at 1 kHz. The magneto – capacitance is defined as[3],

$$MC = \frac{\varepsilon(H) - \varepsilon(0)}{\varepsilon(0)} \times 100, \qquad (5)$$

where ε(H) and ε(0) represent the dielectric constant in the presence and absence of a magnetic field, respectively. The magnetocapacitance value increase with increase in the magnetic field and gradually becomes flat (nearly) at higher field representing saturation[4]. The MC can be positive or negative and the sign of the MC depends on the product of spin – pair correlation of the adjacent spins and the coupling constant. In the present case, it has been found that magnetocapacitance decreases with the increase of the applied magnetic field, which denotes a negative coupling coefficient. Figure S6(b) shows MC effect observed on the thin film under an applied magnetic field of 5 kOe and 1 kHz frequency. The MC value for the thin film was observed to be -2.4 % at 1 kHz, which is comparable with reported MC value for bulk and nano – particles forms of BFO[3]. The observed MC value is attributed to enhanced Bi – O – Fe coordination in thin film composed of sub – 5 nm $BiFeO_3$ nanoparticles.

For the materials exhibiting simultaneous ferroelectric – magnetic ordering, the thermodynamic potential (Φ) can be written as[4]

$$\Phi = \Phi_0 + \alpha P^2 + \frac{\beta}{2} P^4 - PE + \alpha' P^2 + \frac{\beta'}{2} M^4 - MH + \gamma P^2 M^2 \qquad (6)$$

where P and M are the order parameters for the polarization and the magnetization, respectively and $\alpha, \beta, \alpha', \beta'$ and γ are coupling coefficients. The magnetoelectric coupling term P^2M^2 is symmetry independent, expressed as $\Delta\varepsilon \sim \gamma M^2$ with $\Delta\varepsilon = \varepsilon(H) - \varepsilon(0)$. The variation of $\Delta\varepsilon/\varepsilon(0)$ as a function of square of

magnetization $\left(M^2\right)$ is shown in Figure S6(c). The inset in Figure S6(c) shows the variation of M^2 with the applied magnetic field, which shows that $\Delta\varepsilon/\varepsilon$ varies linearly with M^2.

Modeling of Resistive switching behavior

First principles modeling of resistive switching

The observed resistive switching behavior was studied by first principles calculations, which has been recently reported to be a useful tool[5, 6]. The charge trapping, detrapping both the processes are necessary for a reversible RS and symmetrical two – sided NDR. The sudden current jump in the negative bias range in the proximity to ± 0.15 V could be attributed to such a process. The oxidation and redox reactions at defect sites like oxygen vacancies may occur, due to the electro – migrated oxygen ions at the interface.

The density of states (DOS) of the sub – 5 nm $BiFeO_3$ NPs and $BiFeO_3$ unit cell were calculated using Materials Studio 8.0 (Accelrys). Considering the average particle size 2.0 nm, $BiFeO_3$ nanocluster was simulated. For generation of nanocluster, the unit cell of rhombohedral $BiFeO_3$ was built using the lattice parameters $a = b = 5.5182$ Å , $c = 13.7145$ Å and the angular parameters $\alpha = \beta = 90^o$ and $\gamma = 120^o$. The positions of representative atoms within the unit cell are Bi(0, 0, 0), Fe(0, 0, 0.22) and O(0.453, 0.0265, 0.96)[2] (see Figure S7). The spherical shape $BiFeO_3$ nanocluster with diameter 2.0 nm is associated with a cluster of 354 atoms was constructed (see Figure S7). We considered following parameters for the nanocluster generation, (i) the absence of vacancy concentration, (ii) dangling bonds are capped with oxygen atoms and (iii) the radial distribution of cations and anion within the nanocluster. For nanocluster and unit cell, considering the strong Coulomb repulsion (U) between the localized d states of Fe, we choose the $LDA + U$ approach to describe the correlation effects. We used effective Hubbard parameter $U_{eff} = U - J = 4$ eV for Fe atom. The simulation was carried out using

Density Functional Theory Electronic Structure Program (DMol^3). We employed the generalized gradient approximations (GGA) and Perdew – Burke – Ernzerhof (PBE) i.e. PBE – GGA as the exchange and correlation functions. Initially, the simulated BFO nanocluster and unit cell were geometry optimized. In the optimization process, the energy change, force and displacement parameters were set as 1×10^{-5} Ha, 0.002 Ha/Å and 0.005 Å respectively. The optimization was carried out with the step size 0.3 Å. The geometry optimization for both the cases was performed with an All Electron Relativistic core treatment, Double Numerical plus Polarization (DNP+) basis set, Octupole Multipolar expansion. The orbital cutoff scheme was set to Global with a fine quality level calculations and $3 \times 3 \times 3$ k – point mesh. After the geometric optimization, the obtained structure was further employed for the total density of states calculations, with the same core treatment function, basis set, k – point mesh and fine quality calculations as described above.

We carried out first – principles calculations on $BiFeO_3$ nanocluster and bulk $BiFeO_3$ to evaluate NDR process. We have considered three different configurations of the nanocluster namely, nanocluster with no oxygen vacancies, with oxygen vacancies and with the interstitial negatively charged oxygen atoms. The oxygen vacancies in the nanocluster were created by removing oxygen atoms from the nanocluster and the charged oxygen interstitials are realized by inserting an O_2^{2-} into the vacancy sites (see Figure S7).

Figure S7 shows the total density of states obtained on BFO nanocluster for the bulk configuration and above mentioned three different NC configurations. The geometry

followed by energy optimization of a nanocluster without oxygen vacancies shows that the electronic structure of $BiFeO_3$ nanocluster slightly differs compared to bulk $BiFeO_3$.

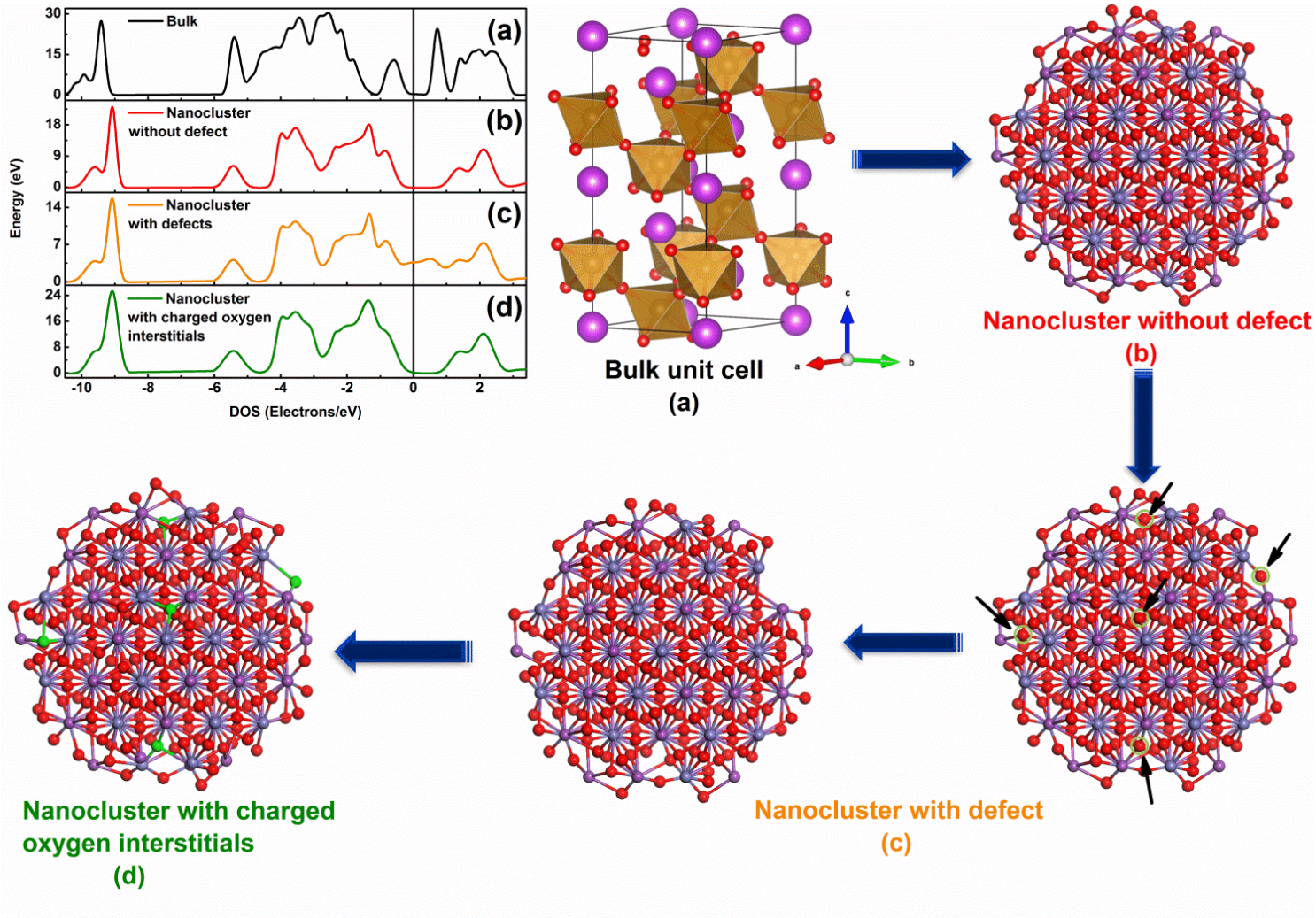

Figure S7 First principles density of study on bulk and nanocluster BFO: (a) total density of state study on bulk BFO unit cell, (b) – (d) shows total density of state studies on BFO nanocluster with different configurations. The Fermi level is set to 0 eV.

Moreover, it can be seen that average Bi – O and Fe – O bond lengths (considering apical, basal and equatorial bonds) are 2.269 Å and 2.054 Å, respectively are nearly 3.5 % larger compared to bulk $BiFeO_3$ (average Bi – O and Fe – O bond lengths are 2.188 Å and 1.985 Å respectively).

The electronic structure of a nanocluster with oxygen vacancies shows that the local structure is affected due to the vacancies, indicating that vacancies are the dominant defect in $BiFeO_3$ nanocluster. Interestingly, it can be seen that with the introduction of oxygen vacancies, nanocluster display half-metallic nature and defect state in the proximity to 0.51 eV arises, which is close to the saturation voltage value of 0.32 V obtained from I – V curves. The calculations show average bond lengths 2.443 Å and 2.278 Å for Bi – O and Fe – O coordination respectively, which are nearly 10 % larger than BFO nanocluster having no vacancies. While, by introducing O_2^{2-} into the vacancy sites, the local structure was observed to be slightly distorted. The average bond lengths for Bi – O and Fe – O coordination were observed to be 2.521 Å and 2.343 Å respectively, which are nearly 16 % larger than nanocluster with no oxygen vacancies. It can be also seen that with the introduction of O_2^{2-} at the vacancy site of nanocluster, the half – metallic and defect state disappears. Thus, we have a transient effect with the introduction of oxygen defects and filling up of the oxygen defects. The charge storage is understood by negative charges fixed at the trapped oxygen atoms and the resistance state of the device transfer to another level, giving rise to NDR effect.

The abrupt current jump observed at a negative and positive voltage is associated with the release of O_2^{2-} from the vacancy sites. The energy barrier (E_b) for this process is calculated as follows,

$$E_b\left(O_2^{2-}\right) = E_{total}\left(\left(BiFeO_3\right)_{NC} + V_O + O_2^{2-}\right) - E_{total}\left(\left(BiFeO_3\right)_{NC} + V_O\right) + E\left(O_2\right) - 2E_f \qquad (7)$$

where $E_{total}\left(\left(BiFeO_3\right)_{NC} + V_O\right)$ is the total energy of the nanocluster containing vacancies, $E_{total}\left(\left(BiFeO_3\right)_{NC} + V_O + O_2^{2-}\right)$ is the total energy of the nanocluster with the vacancies

occupied by O_2^{2-} and $E(O_2)$ is the energy of oxygen molecule and E_f is the Fermi level. The calculated E_b is a function of E_f and observed to be ≈ 0.506 eV, which is very near to the threshold value of 0.51 eV obtained from I – V curve.

Theoretical discussion on electromigration of oxygen ions

The resistive switching phenomenon is commonly attributed to oxygen vacancies. Our elemental analysis shows that the thin film exhibit oxygen vacancies per BFO clusters, additionally oxygen vacancies can be formed during the electroforming process. Thus, after electroformation the stoichiometry of BFO thin film is $BiFeO_{3-x}$.

The Helmholtz layer, which is believed to be formed at $Pt/BiFeO_{3-x}$ interface because of separation of two oppositely charged layers, one is on Pt side and the other is on $BiFeO_{3-x}$ side. The electroforming process lead to the incorporation of oxygen in Pt electrode by chemisorption or physisorption processes most probably at grain boundaries[7]. We postulate that the oxygen atoms in Pt electrode can governed voltage controlled creation and annihilation of oxygen vacancies at a $Pt/BiFeO_{3-x}$ interface. Using Kröger – Vink notation, an oxygen – vacancy annihilation reaction on $BiFeO_{3-x}$ side of the interface is given by

$$O_{\circ}^{*}(\mathrm{Pt}) + V_{\circ}^{\bullet\bullet}(BiFeO_{3-x}) \rightarrow V_{\circ}^{\bullet\bullet}(\mathrm{Pt}) + O_{\circ}^{*}(BiFeO_{3-x}), \qquad (8)$$

The reverse of Equation (8) gives oxygen – vacancy formation reaction on $BiFeO_{3-x}$ side. With reference to the formation free energy of Equation (8), the reaction can be divided into three reactions:

$$O_{\circ}^{*}(\mathrm{Pt}) \rightarrow V_{\circ}^{\bullet\bullet}(\mathrm{Pt}) + 2e^{-}(\mathrm{Pt}) + 1/2\,O_{2(g)}, \qquad (9)$$

$$1/2\,O_{2(g)} + V_{\circ}^{\bullet\bullet}(BiFeO_{3-x}) + 2e^{-}(BiFeO_{3-x}) \rightarrow O_{\circ}^{*}(BiFeO_{3-x}), \qquad (10)$$

and

$$e^{-}(\mathrm{Pt}) \rightarrow e^{-}(BiFeO_{3-x}). \qquad (11)$$

A change in energy of Equation (11) can be determined from the work – function difference between Pt and $BiFeO_{3-x}$. After the electroformation, the Fermi energy of

$BiFeO_{3-x}$ is believed to be very close to the conduction band minimum. Thus, the work – function difference between Pt and $BiFeO_{3-x}$ is $\phi_{Pt} - \chi BiFeO_{3-x}$, where ϕ_{Pt} and $\chi BiFeO_{3-x}$ are the work function of Pt and electron affinity of $BiFeO_{3-x}$, respectively. Thus, energy for Equation (11) is equal to $\phi_{Pt} - \chi BiFeO_{3-x}$.

Numerical analysis of Resistive switching

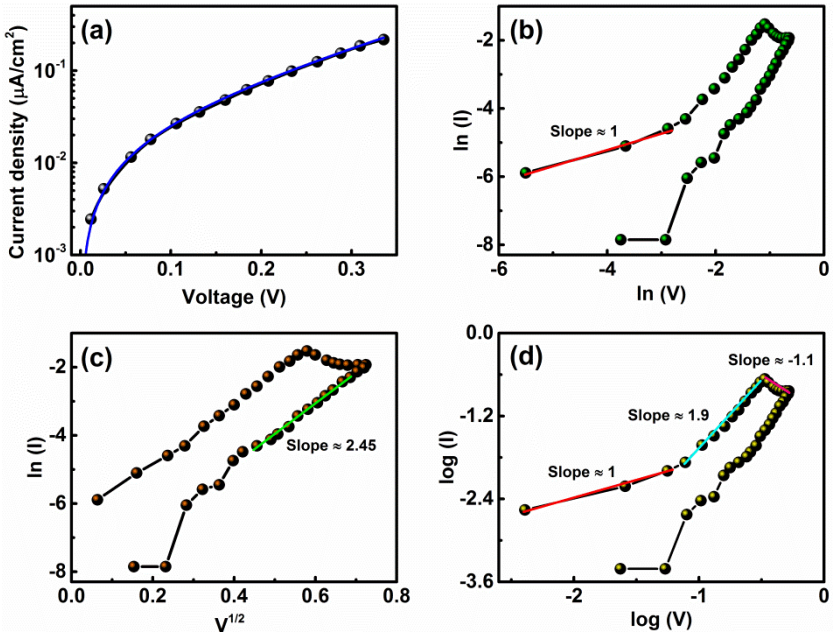

Figure S8 (a) Simmon's model fitting in the positive I – V region of the device, the blue color line shows fitting using model, (b) – (d) numerical analysis of RS mechanism representing conduction types.

In order to elucidate more information on BRS mechanism, we performed numerical analysis of the BRS (see Figure S8(a) – (d)). The electron tunneling process with the device can be modeled using Simmons model combined with Wentzel – Kramers – Brillouin (WKB) approximation. The tunneling current in the electron tunneling regime can be expressed using the following function[8]:

$$J = \frac{e}{2\pi\hbar d_i^{\,2}} \left\{ \begin{array}{l} \left(e\phi_b - \frac{eV}{2} \right) \times \exp\left[\frac{4\pi d_i}{h} (2m_e)^{1/2} \zeta \left(e\phi_b - \frac{eV}{2} \right)^{1/2} \right] \\ -\left(e\phi_b + \frac{eV}{2} \right) \times \exp\left[\frac{4\pi d_i}{h} (2m_e)^{1/2} \zeta \left(e\phi_b + \frac{eV}{2} \right)^{1/2} \right] \end{array} \right\} \qquad (8)$$

this equation gives the relationship between current density and applied bias. The parameters, ϕ_b and d_i represent a barrier height and thickness respectively, which are the main parameters that affects the tunneling of electrons through a barrier; ζ is a unitless

parameter used for fitting, m_e is the rest mass of an electron, e is the electronic charge and h is Planck's constant. Figure S8(a) shows approximately good fit between experimental data and Simmons' model with Helmoltz layer thickness 1.29 nm and the parameters ϕ_b and ζ were estimated to be 1.37 nm and 0.78 respectively. Moreover, it can be seen from Figure S8(b) that in the LRS state, I – V follows Ohmic behavior with slope ≈ 1. The HRS state of I – V exclusively fitted well with the relation $\ln(I) \text{vs} V^{1/2}$ with slope ≈ 2.45 and indicates Schottky emission (Figure S8(c)). The log – log plot of I – V curve shows that at high voltage region the slope of curve is negative with the value ≈ - 1.1, indicating NDR characteristic (Figure S8(d)). Thus, the overall RS mechanism occurs due to the combination and interplay between several linear and non – linear conduction of mechanisms.

References

1. J. Hyeon-Lee, G. Beaucage, S. E. Pratsinis and S. Vemury, *Langmuir*, 1998, 14, 5751-5756.
2. M. M. Shirolkar, X. Dong, J. Li, S. Yin, M. Li and H. Wang, *Phys Chem Chem Phys*, 2016, 18, 25409-25420.
3. M. M. Shirolkar, C. Hao, X. Dong, T. Guo, L. Zhang, M. Li and H. Wang, *Nanoscale*, 2014, 6, 4735-4744.
4. M. Rawat and K. L. Yadav, *Smart Materials and Structures*, 2014, 23, 085032.
5. B. Magyari-Köpe, M. Tendulkar, S.-G. Park, H. D. Lee and Y. Nishi, *Nanotechnology*, 2011, 22, 254029.
6. Y. Yang and W. Lu, *Nanoscale*, 2013, 5, 10076.
7. D. S. Jeong, H. Schroeder and R. Waser, *Physical Review B*, 2009, 79.
8. J. G. Simmons, *Journal of Applied Physics*, 1963, 34, 1793-1803.